JOURNAL OF SOLID STATE CHEMISTRY

Volume 179, Number 7, July 2006

CONTENTS

Regular Articles

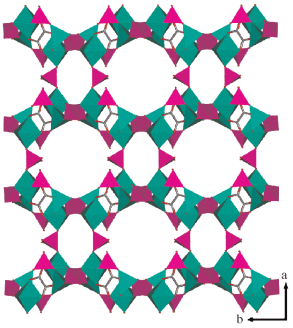

Compound **4** contains layers where the $Ga_4(PO_4)_4(C_2O_4)$ building units are connected to each other in an opposite orientation. The phosphorous atom sits on a twofold axis, is positioned between the layers and joins the $GaO_4(C_2O_4)$ group from adjacent layers, generating two types of alternating 8MR and 12MR channels along the [001] direction.

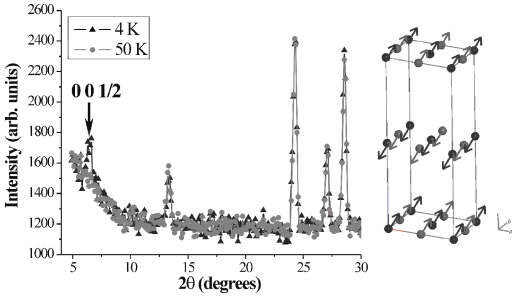

Powder neutron diffraction pattern of $La_5Re_3NiO_{16}$ showing the new $(0\,0\,1/2)$ magnetic reflection. The inset shows the unusual magnetic structure, which has ferromagnetic intralayer coupling between Re (black spheres, black arrows) and Ni (grey spheres, grey arrows), whose moments are angled 45° in the *ab* plane and canted 30° from the *c*-axis, and antiferromagnetic interplanar coupling.

Regular Articles—Continued

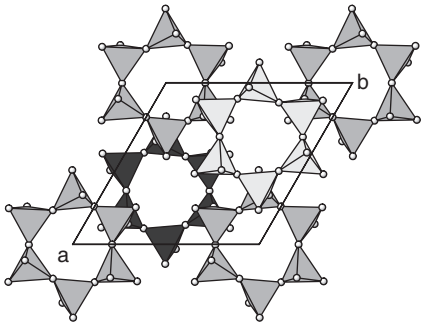

Sequence of six-membered tetrahedral rings within the interrupted framework.

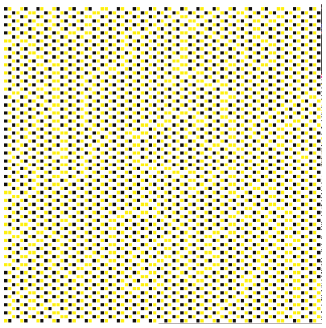

Monte Carlo simulation of the $Q_4(m\mathrm{Al})$ silicon connectivity in the α-hexagonal celsian lattice, for a Si/Al ratio of 1:1. Si atoms are shown in yellow and the Al atoms in black.

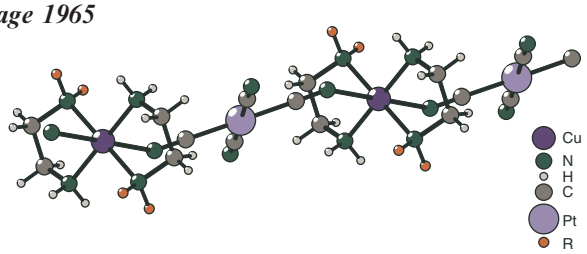

Chain-like structure in $[Cu(en)_2][Pt(CN)_4]$ (R = H) and $[Cu(dmen)_2][Pt(CN)_4]$ (R = CH_3) compounds.

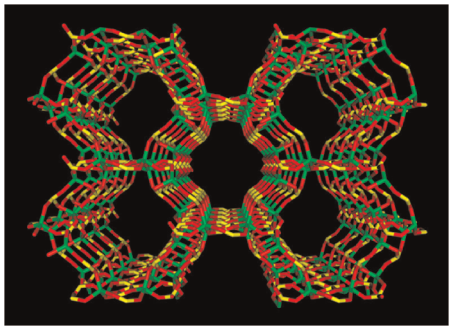

View of the structure of **1** along the [001] direction showing the 16-ring channels.

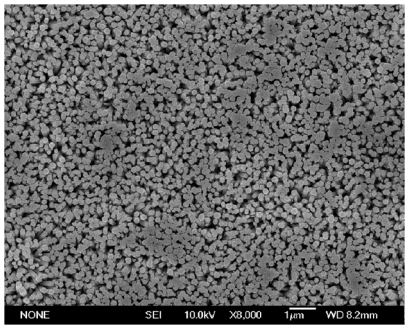

SEM image of the array; this image is representative of the entire surface.

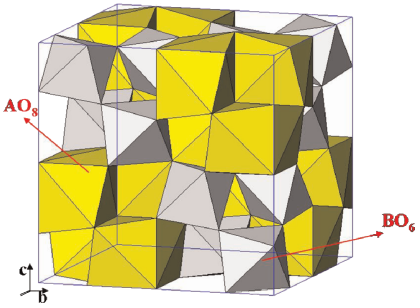

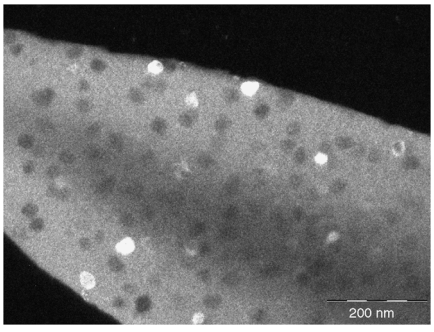

TEM image of an oxyfluoride glass-ceramic containing Er^{3+}-doped β-PbF_2 nanocrystals.

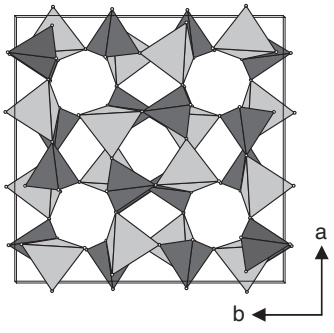

Crystal structure of $CuReO_4$ with tetrahedral coordination of Cu(I) and Re(VII) atoms represents a new structure type related to some silicon dioxides.

Continued

Yb–Zn–Al ternary system: $CaCu_5$-type derived compounds in the zinc-rich corner
Maria Luisa Fornasini, Pietro Manfrinetti and Donata Mazzone
Page 2012

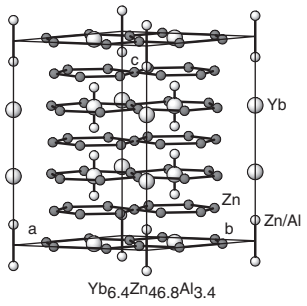

A new $CaCu_5$-type derived structure with a nine times large volume.

Preparation and properties of amorphous titania-coated zinc oxide nanoparticles
Min-Hung Liao, Chih-Hsiung Hsu and Dong-Hwang Chen
Page 2020

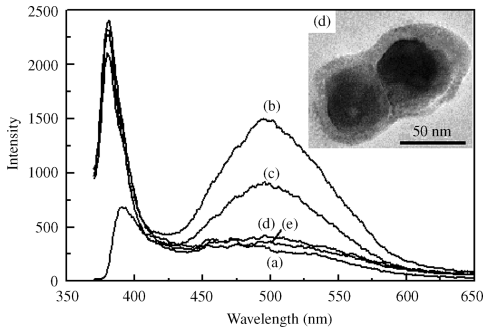

Amorphous titania-coated ZnO nanoparticles with a core-shell structure were prepared. It was found that the emission intensity of ZnO cores could be significantly enhanced by the amorphous TiO_2 shell.

A controlled release of ibuprofen by systematically tailoring the morphology of mesoporous silica materials
Fengyu Qu, Guangshan Zhu, Huiming Lin, Weiwei Zhang, Jinyu Sun, Shougui Li and Shilun Qiu
Page 2027

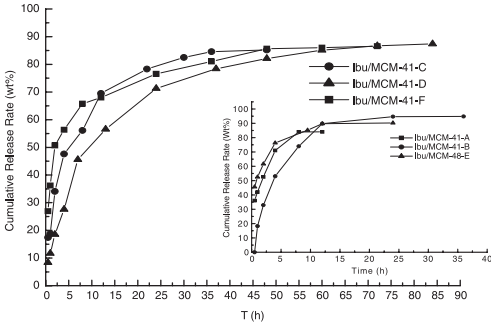

Cumulative release rates of ibuprofen from variable morphologies of mesoporous silica.

Growth of La_2CuO_4 nanofibers under a mild condition by using single walled carbon nanotubes as templates
Lizhen Gao, Xiaolin Wang, Hui Tong Chua and Sibudjing Kawi
Page 2036

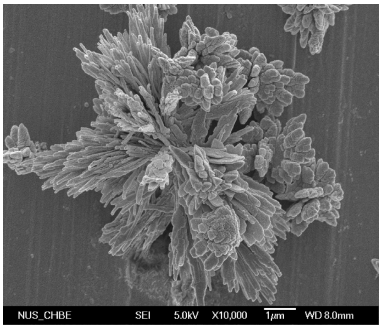

La_2CuO_4 nanofibers have been grown *in situ* by using single walled carbon nanotubes as templates under mild hydrothermal conditions and a temperature around 60 °C. The La_2CuO_4 crystals grew from needle-like (5 h) through stick-like (20 h) and finally to plate-like (40 h) fibers. The La_2CuO_4 nanofibers are probably cubic rather than round and may capsulate SWNTs.

Crystal structure and specific heat of GdCuGe
Sudhindra Rayaprol, C. Peter Sebastian and Rainer Pöttgen
Page 2041

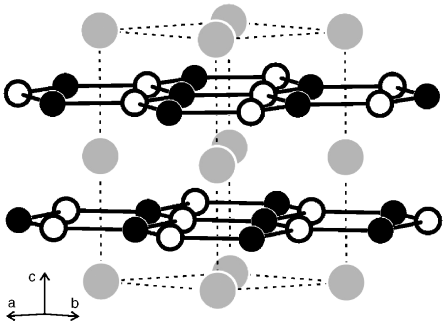

Crystal structure of GdCuGe. The gadolinium, copper, and germanium atoms are drawn as medium gray, black filled, and open circles, respectively. The two-dimensional [CuGe] networks are emphasized.

Structure and thermoelectric properties of the ordered skutterudite $CoGe_{1.5}Te_{1.5}$
Paz Vaqueiro, Gerard G. Sobany, A.V. Powell and Kevin S. Knight
Page 2047

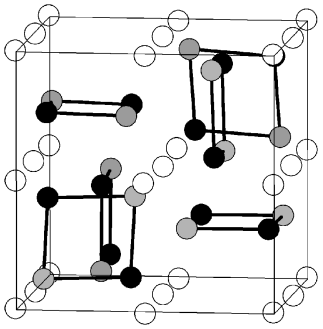

$CoGe_{1.5}Te_{1.5}$ exhibits an ordered skutterudite structure, in which the anions are ordered in layers perpendicular to the [111] direction.

Synthesis, crystal structure and magnetic properties of an alternating manganese chain

Manuela Ramos Silva, Ana Matos Beja, José António Paixão and Jesus Martín-Gil

Page 2054

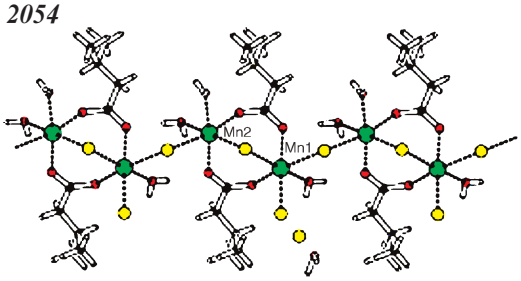

Portion of the dimeric manganese chain showing the two alternating exchange interactions paths.

From chemistry to materials, design and photophysics of functional terbium molecular hybrids from assembling covalent chromophore to alkoxysilanes through hydrogen transfer addition

Bing Yan and Dong-Jie Ma

Page 2059

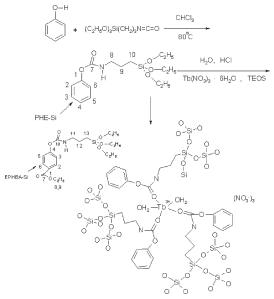

The active hydroxyl groups of phenol/ethyl-*p*-hydroxybenzoate grafted by 3-(triethoxysilyl)-propyl isocyanate (TESPIC) through hydrogen transfer reaction were used as multi-functional bridged components, which can coordinate to Tb^{3+} with carbonyl groups, strongly absorb ultraviolet and effectively transfer energy to Tb^{3+} through their triplet excited state, as well as undergo polymerization or crosslinking reactions with tetraethoxysilane (TEOS), for anchoring terbium ions to the silica backbone with covalently bonded.

Anion substitution effects on structure and magnetism of the chromium chalcogenide Cr_5Te_8—Part II: Cluster-glass and spin-glass behavior in trigonal $Cr_{(1+x)}$ Q_2 with basic cells and trigonal $Cr_{(5+x)}$ Q_8 with superstructures (Q = Te, Se; Te:Se = 6:2)

Zhong-Le Huang, Wolfgang Bensch, Sergiy Mankovsky, Svitlana Polesya, Hubert Ebert and Reinhard K. Kremer

Page 2067

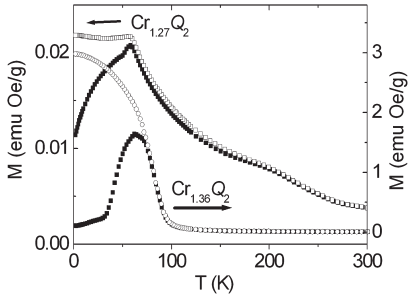

Temperature-dependent M_{ZFC} and M_{FC} with $H = 100$ Oe for $Cr_{1.27}Q_2$ and $Cr_{1.36}Q_2$.

Magnetic susceptibility and specific heat of uranium double perovskite oxides Ba_2MUO_6 (M = Co, Ni)

Yukio Hinatsu and Yoshihiro Doi

Page 2079

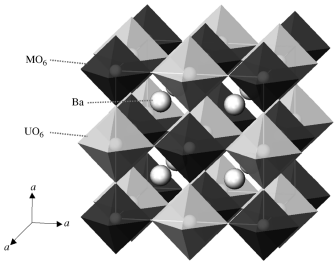

The crystal structure for Ba_2CoUO_6 and Ba_2NiUO_6. They crystallize in the cubic double perovskite-type structure and order ferromagnetically at 9.1 and 25 K, respectively.

Crystallographic and magnetic properties of $CaLaMnMoO_6$ double perovskite

Qisheng Lin, Martha Greenblatt, El'ad N. Caspi and Maxim Avdeev

Page 2086

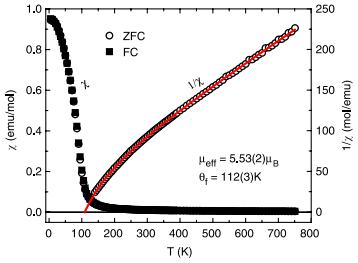

Temperature-dependent magnetic susceptibility, χ and inverse susceptibility, $1/\chi$ for the double perovskite, $CaLaMnMoO_6$ at $H = 10$ kOe. Solid line is a fit of the ferrimagnetic modified Curie–Weiss model, $1/\chi = T/C + 1/\chi_0 - \sigma/T - \theta$ to the inverse susceptibility data.

Synthesis and characterization of one- to three-dimensional compounds composed of paradodecatungstate-B cluster and transition metals as linkers

Chun-Yan Sun, Shu-Xia Liu, Lin-Hua Xie, Chun-Ling Wang, Bo Gao, Chun-Dan Zhang and Zhong-Min Su

Page 2093

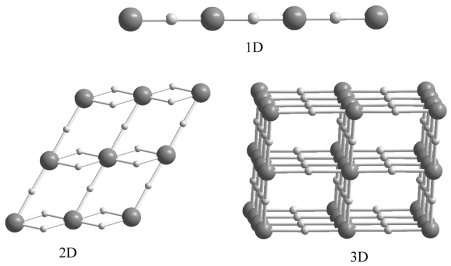

Three new compounds with one- to three-dimensional extended frameworks built from $[H_2W_{12}O_{42}]^{10-}$ anion and transition metals have been synthesized and characterized by elemental analyses, X-ray single-crystal analyses, magnetic measurement, XRPD, and cyclic voltammetry measurements. The cobalt containing compound exhibits interesting reversible sorption/desorption of water molecules.

Continued

$Sr_4PbPt_4O_{11}$, the first platinum oxide containing Pt_2^{6+} ions

Catherine Renard, Pascal Roussel, Annick Rubbens, Sylvie Daviero-Minaud and Francis Abraham

Page 2101

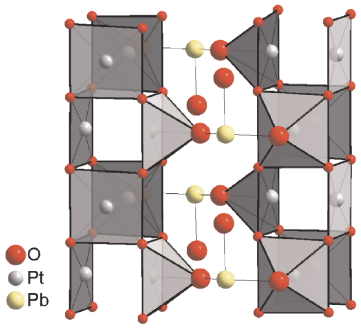

The structure of $Sr_4PbPt_4O_{11}$ is built from $[Pt_4O_{10}{}^{8-}]_\infty$ columns connected by lead atoms. Pt_2^{6+} ions are created between PtO_4 square plane and PtO_5 square pyramid.

Structural and ^{31}P NMR investigation of $Bi(MM')_2PO_6$ statistic solid solutions: Deconvolution of lattice constraints and cationic influences

Marie Colmont, Laurent Delevoye, El Mostafa Ketatni, Lionel Montagne and Olivier Mentré

Page 2111

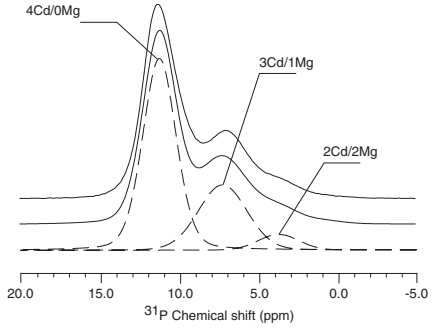

First $(CdMg)_4$ cationic sphere influence on the ^{31}P NMR signal in $Bi(Cd,Mg)_2PO_6$.

Electronic, magnetic and structural properties of A_2VMoO_6 perovskites (A = Ca, Sr)

P. Karen, A.R. Moodenbaugh, J. Goldberger, P.N. Santhosh and P.M. Woodward

Page 2120

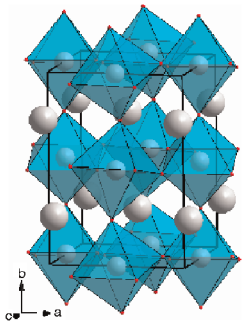

Unit cell of $Ca(V_{0.5}Mo_{0.5})O_3$.

Origin of stability of the high-temperature, low-pressure Rh_2O_3 III form of rhodium sesquioxide

Shuping Zhuo and Karl Sohlberg

Page 2126

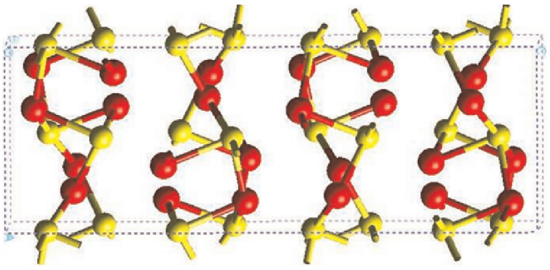

Calculations of the Gibbs free energies for three phases of Rh sesquioxide, including estimates of the vibrational energy and vibrational entropy contributions, show that this Rh_2O_3 III phase is entropically stabilized.

A series of spinel phase cathode materials prepared by a simple hydrothermal process for rechargeable lithium batteries

Yan-Yu Liang, Shu-Juan Bao and Hu-Lin Li

Page 2133

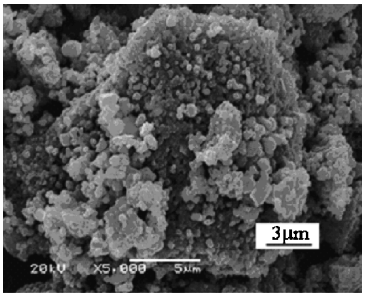

It is a SEM image of the spinel $LiMn_2O_4$, which was prepared by this novel hydrothermal procedure. It illustrates that reasonable-crystallized spinel oxide has occurred through the special hydrothermal process and the average particle size declined to about 1 μm. This homogeneous grain size distribution provides an important morphological basis for the reversibility and accessibility of lithium ion insertion/extraction reactions.

Crystal chemistry on a lattice: The case of BZN and BZN-related pyrochlores

Yun Liu, Ray L. Withers, T.R. Welberry, Hong Wang and Huiling Du

Page 2141

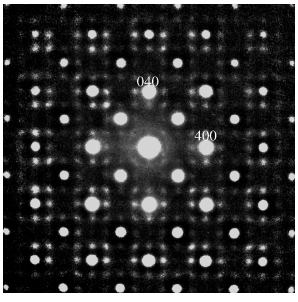

A typical 〈00l〉 zone axis EDP of $(Bi_{1.5}Zn_{0.5})(Ti_{1.5}Nb_{0.5})O_7$ (BZNT).

Synthesis and crystal structure of $Mg_2B_{24}C$, a new boron-rich boride related to "tetragonal boron *I*"
Volker Adasch, Kai-Uwe Hess, Thilo Ludwig, Natascha Vojteer and Harald Hillebrecht
Page 2150

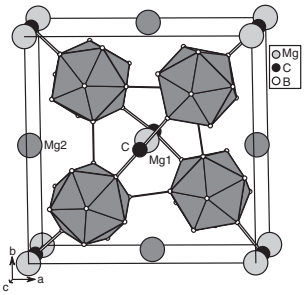

$Mg_2B_{24}C$, a new boron-rich boridecarbide of magnesium, was synthesized from the elements. Its crystal structure is closely related to "tetragonal boron *I*" and can be described as a tetragonal rod packing of corner-linked B_{12} icosahedra with C and Mg atoms in the voids. $Mg_2B_{24}C$ is the first example for a compound related to "tetragonal boron *I*" with a stoichiometric composition.

Thermoelectric and structural properties of a new Chevrel phase: $Ti_{0.3}Mo_5RuSe_8$
Michael A. McGuire, Anneliese M. Schmidt, Franck Gascoin, G. Jeffrey Snyder and Francis J. DiSalvo
Page 2158

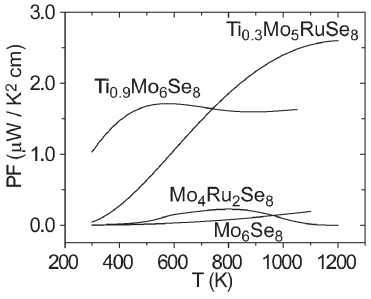

A combination of Ti-filling and Ru-substitution in Chevrel phase selenides has been investigated. The compound $Ti_{0.3}Mo_5RuSe_8$ was synthesized, and its electrical resistivity (ρ) and Seebeck coefficient (S) were measured up to 1200 K. Comparison of the thermoelectric power factor ($PF = S^2/\rho$) shows that this material performs better than both the Ti-filled phase $Ti_{0.9}Mo_6Se_8$ and the fully Ru-substituted phase $Mo_4Ru_2Se_8$.

Structural and conductivity studies of $CsKSO_4Te(OH)_6$ and $Rb_{1.25}K_{0.75}SO_4Te(OH)_6$ materials
N. Chabchoub, J. Darriet and H. Khemakhem
Page 2164

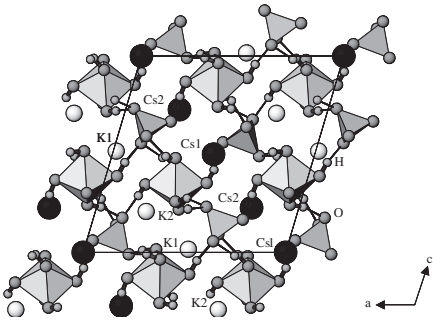

Projection of $CsK(SO_4)\cdot Te(OH)_6$ crystal structure on the *ac* plane.

Effect of iron-doping on spin-state transition and ferromagnetism in $Pr_{0.5}Ca_{0.5}CoO_{3-\delta}$ cobalt oxides
X.G. Luo, X. Li, G.Y. Wang, G. Wu and X.H. Chen
Page 2174

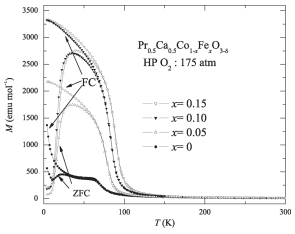

The article reported the influence of the iron-doping on the spin-state transition and ferromagnetism in $Pr_{0.5}Ca_{0.5}CoO_{3-\delta}$ system. It is found that the oxygen vacancy leads to an incomplete spin-state transition (SST), while the iron-doping destroys the SST. Another effect of the iron-doping is that the ferromagnetism of the system is enhanced with Fe doping. These results could be interpreted by taking in account the change of the crystal lattice by the variation of oxygen content and the Fe doping.

Evaluation of the acid properties of porous zirconium-doped and undoped silica materials
D. Fuentes-Perujo, J. Santamaría-González, J. Mérida-Robles, E. Rodríguez-Castellón, A. Jiménez-López, P. Maireles-Torres, R. Moreno-Tost and R. Mariscal
Page 2182

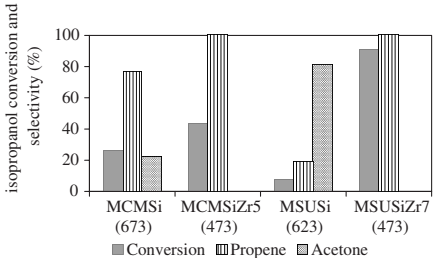

The adsorption of basic probe molecules and the catalytic behaviour have revealed that MSU-type materials are more acidic than the analogous MCM-41 solids, mainly after the incorporation of zirconium into the silica framework.

As–As dimerization, Fermi surfaces and the anomalous electrical transport properties of UAsSe and ThAsSe
Ray L. Withers, Herman J.P. van Midden, Albert Prodan, P.A. Midgley, J. Schoenes and R. Vincent
Page 2190

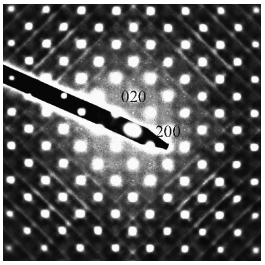

A typical ⟨001⟩ zone axis EDP of UAsSe taken at ~80–90 K. In addition to the strong Bragg reflections of the underlying *P4/nmm* average structure, note the presence of a highly structured characteristic diffuse intensity distribution arising from disordered As–As dimerization.

Continued

Stable cubic spinels in the Zn–Mn–O system in air
J. Blasco and J. García
Page 2199

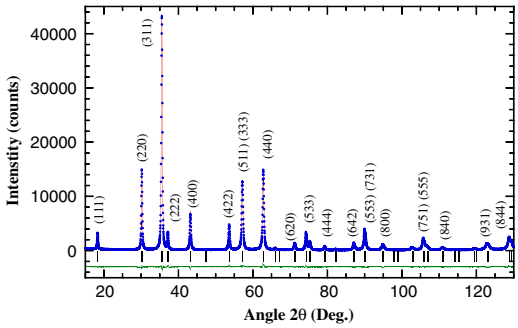

X-ray refinement for $Mn_{1.3}Zn_{1.7}O_4$ sintered at 600 °C during 15 h. Representative reflections are also indicated in the figure.

Control of retention and fatigue-free characteristics in $CaBi_4Ti_4O_{15}$ thin films prepared by chemical method
A.Z. Simões, M.A. Ramírez, A.H.M. Gonzalez, C.S. Riccardi, A. Ries, E. Longo and J.A. Varela
Page 2206

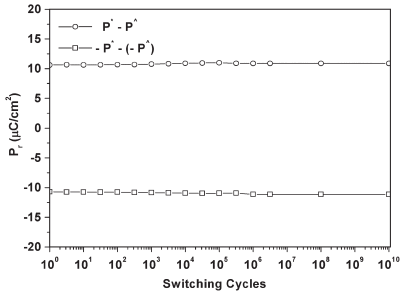

Fatigue of CBTi144 thin film obtained by polymeric precursor method.

Systems *R*–Fe–O (*R* = Ho, Er): Thermodynamic properties of ternary oxides using differential scanning calorimetry and solid-state electrochemical cells
S.C. Parida, S.K. Rakshit, S. Dash, Ziley Singh, B.K. Sen and V. Venugopal
Page 2212

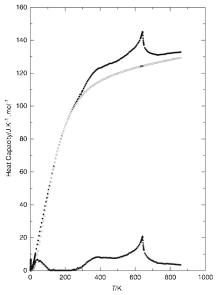

Plot of heat capacity against temperature for $HoFeO_3$(s) showing different contributions: (●) total heat capacity; (○) lattice contribution; and (▲) magnetic contribution.

Structural and magnetic properties of high-pressure/high-temperature synthesized $(Sr_{1-x}R_x)CoO_3$ (R = Y and Ho) perovskites
S. Balamurugan and E. Takayama-Muromachi
Page 2231

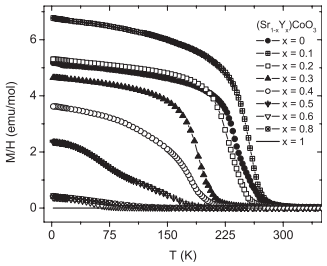

Temperature dependence of M/H for the $Sr_{1-x}Y_xCoO_3$ system measured at an applied field of 1 kOe by the field-cooling mode.

Rapid Communications

Correlation of reactivity with structural factors in a series of Fe(II) substituted cobalt ferrites
Elsa E. Sileo, Luis García Rodenas, Carlos O. Paiva-Santos, Peter W. Stephens, Pedro J. Morando and Miguel A. Blesa
Page 2237

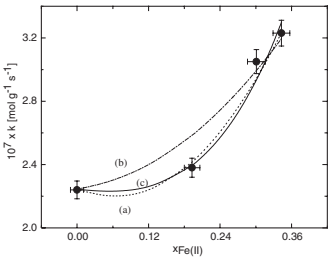

The electron exchange between octahedral Fe^{II} and Fe^{III} ions has important consequences on the specific dissolution rates.

High-pressure synthesis and single-crystal structure refinement of gadolinium holmium silicate hydroxyapatite $Gd_{4.33}Ho_{4.33}(SiO_4)_6(OH)_2$
Chao Wang, Xiaoyang Liu, M.E. Fleet, Shouhua Feng and Ruren Xu
Page 2245

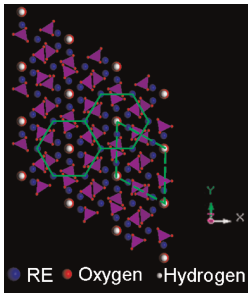

Crystal structure of double *RE* hydroxyapatite $Gd_{4.33}Ho_{4.33}(SiO_4)_6(OH)_2$ along [001] direction. *RE*(2) atoms define the apatite channel and are, in turn, enclosed by a hexagon of *RE*(1).

NOTICE

The Keyword Index for Volume 179 will appear in the December 2006 issue as part of a cumulative index for the year 2006.